Volume 20 | Number 46 | 14 December 2018 | Pages 28945–29570

PCCP

Physical Chemistry Chemical Physics

rsc.li/pccp

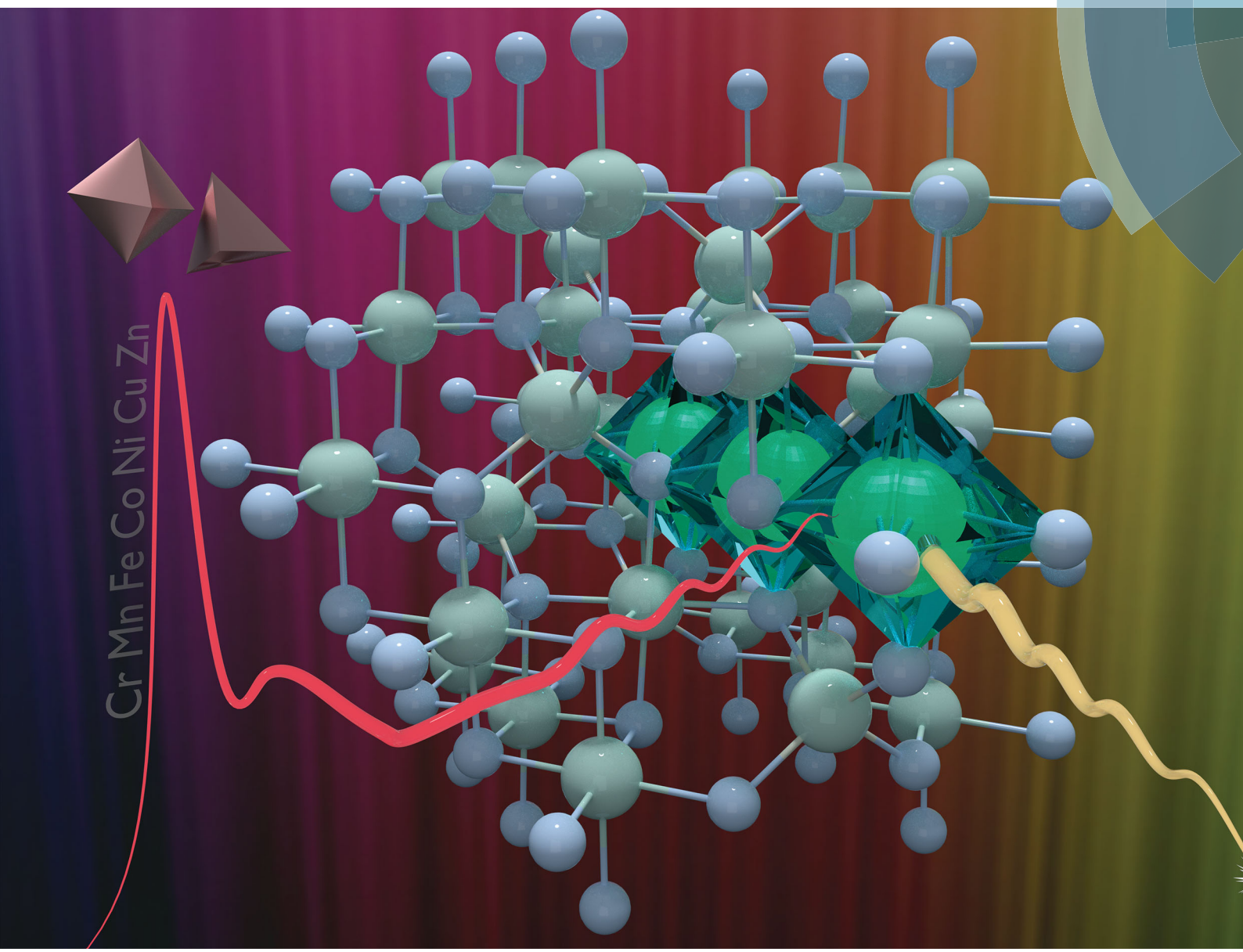

ISSN 1463-9076

ROYAL SOCIETY OF CHEMISTRY

PAPER

Richard D. Robinson *et al.*

X-ray emission spectroscopy: an effective route to extract site occupation of cations

PCCP

PAPER

Check for updates

Cite this: *Phys. Chem. Chem. Phys.*, 2018, **20**, 28990

X-ray emission spectroscopy: an effective route to extract site occupation of cations†

Anuj Bhargava, [a] Cindy Y. Chen, [a] Kenneth D. Finkelstein, [b] Matthew J. Ward [bc] and Richard D. Robinson [*a]

Received 20th July 2018,
Accepted 15th September 2018

DOI: 10.1039/c8cp04628j

rsc.li/pccp

Cation site occupation is an important determinant of materials properties, especially in a complex system with multiple cations such as in ternary spinels. Many methods for extracting the cation site information have been explored in the past, including analysis of spectra obtained through K-edge X-ray absorption spectroscopy (XAS). In this work, we measure the effectiveness of X-ray emission spectroscopy (XES) for determining the cation site occupation. As a test system we use spinel phase $Co_xMn_{3-x}O_4$ nanoparticles contaminated with CoO phases because Co and Mn can occupy all cation sites and the impurity simulates typical products of oxide syntheses. We take advantage of the spin and oxidation state sensitive $K\beta_{1,3}$ peak obtained using XES and demonstrate that XES is a powerful and reliable technique for determining site occupation in ternary spinel systems. Comparison between the extended X-ray absorption fine structure (EXAFS) and XES techniques reveals that XES provides not only the site occupation information as EXAFS, but also additional information on the oxidation states of the cations at each site. We show that the error for EXAFS can be as high as 35% which makes the results obtained ambiguous for certain stoichiometries, whereas for XES, the error determined is consistently smaller than 10%. Thus, we conclude that XES is a superior and a far more accurate method than XAS in extracting cation site occupation in spinel crystal structures.

Introduction

Understanding the distribution of cations in the sublattice sites of a material is of great importance due to the profound effects that cation distribution induces on a material's optical, catalytic, magnetic, and electronic properties.[1–4] In certain systems, the anion sublattice can be static while the cation distribution can vary. This rearrangement of cations can lead to dramatic changes in properties. For example, in the spinel system of $MnCo_2O_4$, as the Co and Mn atoms are shuffled between octahedral and tetrahedral sites, the activity of the oxidation–reduction reaction dramatically changes.[5] Similarly, the elucidation of cation distribution has been widely explored to understand the role of cation rearrangement in materials employed in technological applications such as photodetectors,[6] transparent conducting films,[7] electrocatalysts,[8] and electrochemical energy storage devices.[9] While the dependence of material properties on the cation distribution has been found in many materials, because there is substantial interplay among atom types, oxidation states, and sites, the extraction and prediction of cation distribution is especially important for ternary spinel oxides.

In ternary spinels, the cation distribution can be expressed as $(A_tB_{1-t})[A_xB_{2-x}]O_4$ $(0 < t < 1$ and $0 < x < 2)$ where there are two sites for the A and B cations: tetrahedral (T_d) and octahedral [O_h], the sites being designated by the brackets () and [], respectively. Frequently in the spinel systems, the A and B cations can be freely distributed between the O_h and T_d sites, with the cation site disorder being influenced by various crystal chemical and processing factors such as ion size, oxidation state, crystal field stabilization energy, synthesis and processing temperature, and oxygen partial pressure.[10–16] But the site disorder includes not only the atom type but the oxidation state as well, as observed in the case of, for example, the spinel cobalt manganese oxide system, in which Co^{3+} and Mn^{3+} cations are present at O_h sites, and Co^{2+} and Mn^{2+} cations are present at both T_d and O_h sites. This stoichiometric-dependent and processing-dependent disorder[16] makes it difficult to understand the fundamental properties of a compound. Knowledge of this oxidation-state site occupation is important, for instance, when looking at the electronic conductivity in spinel oxides. In spinel oxides it is known that the most prominent mechanism of charge transport is through small polaron nearest neighbour hopping (NNH),[17,18] a process in which charge carriers move from one

[a] *Department of Materials Science and Engineering, Cornell University, Ithaca, NY 14853, USA. E-mail: rdr82@cornell.edu*
[b] *Cornell High Energy Synchrotron Source (CHESS), Cornell University, Ithaca, NY 14853, USA*
[c] *CLS@APS, Sector 20 Advanced Photon Source, Canadian Light Source Inc., S44 Innovation Boulevard, Saskatoon, SK S7N 2V3, Canada*

† Electronic supplementary information (ESI) available. See DOI: 10.1039/c8cp04628j

This journal is © the Owner Societies 2018

O_h cation site to another *via* the energy it receives by coupling to lattice vibrations. Hence, the electrical conductivity in spinels is directly proportional to the number of electron donor/acceptor hopping pairs M^{2+}/M^{3+}, where M is the cation present at O_h sites.[16,19–21] But the polaron hopping models are too crude to account for the cation configurational differences that occur in ternary transition metal spinels. As a consequence, the relationship between cation site occupation and properties—such as electrochemical behaviour and electrical conductivity—has not been characterized for ternary oxides, complicating efforts to design new materials for use in applications such as in electrochemical energy storage and conversion devices.

There are several methods to determine site occupation of each cation species in a material, with some being more accessible than others. Neutron diffraction is the standard bearer for this type of analysis,[11] in which the Rietveld refinement of the data yields the cation distributions, but neutron sources are rare. Additionally, extremely accurate form factors are required to extract the oxidation states, therefore, it may not be possible to use Rietveld refinement for systems with small crystal grains or lack of long range order, like nanoparticles (NP).[22] X-ray photoelectron spectroscopy can be used to determine the relative concentration of a species of an atom having different oxidation states,[23] but it does not provide the site information, *i.e.*, T_d or O_h sites in spinels, for each cation species. Alternatively, one could utilize the high-energy X-ray characterization methods such as K-edge X-ray absorption spectroscopy (XAS) and X-ray emission spectroscopy (XES) that can probe local environments around a target atom type. XAS is a powerful tool to study the electronic and geometric structure of materials through both X-ray absorption near-edge structure (XANES) and extended X-ray absorption fine structure (EXAFS).[24–29] Analysis of the XANES spectra can provide the oxidation states of the metal centres, and EXAFS is useful for studying the local short-range structure around the central absorbing atom, and provides the interatomic distances and the coordination numbers for the neighbouring atoms. While EXAFS and XANES are both valuable techniques, they also have limitations when used to assess the site occupation of cations. One such limitation is that although the absorption spectra obtained using XAS is element specific, it only yields information on the average of all the oxidation states of the element, hindering the understanding of how different central absorbing atoms affect the oxidation state, coordination environment, or occupation at different sites in a polyhedra.[30] For instance, in cobalt manganese oxide, if Co atoms are present as Co^{2+} at T_d sites, and Co^{2+} and Co^{3+} at O_h sites, the Co K-edge EXAFS would only be able to provide the ratio of Co atoms present at T_d and O_h sites but not the ratio of Co^{2+} and Co^{3+} cations occupying O_h sites, rendering this technique insufficient for such detailed analysis. Although a combination of XANES and EXAFS analyses can be used to determine the site occupation of all cation species for simple systems like binary spinel oxides, XAS may not be sufficient to provide the complete site occupation data for more complex systems like ternary spinel oxides due to the large number of variables associated with mixed site occupation and oxidation states which make the EXAFS errors predominant and large. In this work we find that the large number of fitting parameters associated with the EXAFS analysis render the error in site occupation to be as high as 35%, as discussed later. Errors can also be introduced with XANES because the K-edge is sensitive to the ligand environment as well as the oxidation state of the absorbing atom.[31] For example, for a fixed Mn oxidation state the XANES edge energy can shift in the range of 0.5–2.0 eV.[32] Since the oxidation states of the sample are determined assuming a linear relationship between the oxidation state and edge energy of the standards, this introduces another error in the determination of the oxidation state of the samples. Consequently, the combination of errors associated with both XANES and EXAFS can lead to high uncertainty in the site occupation of cations, especially for complex systems. Since properties such as polaron charge hopping rely on correlating the site occupation parameters to understand the mechanism, it is essential to extract the site occupation and concentration of all cation species ($Co_{T_d}^{2+}$, $Co_{O_h}^{2+}$, $Co_{O_h}^{3+}$, $Mn_{T_d}^{2+}$, $Mn_{O_h}^{2+}$, $Mn_{O_h}^{3+}$) in the spinel structure. Therefore, it becomes imperative to develop a technique which can reliably determine the oxidation state and site occupation of cations in complex systems.

In this work, we take advantage of the spin, ligand geometry, and oxidation state sensitive $K\beta_{1,3}$ ($3p \rightarrow 1s$) peak obtained using XES to study the geometric structure of spinel phase NP which are contaminated with other impure oxide phases. We focus on nanoparticles since these are the major form researched in emerging applications.[9,33–36] We demonstrate that XES can be used reliably as a technique for extracting the concentration of cations having different ligand geometries (coordination), site occupation, and oxidation states. Furthermore, we compare the site occupation of cations obtained using XES to the results from EXAFS, and demonstrate that while both techniques reach similar findings, XES is superior since it provides not only the elemental site occupation as EXAFS, but also oxidation state site occupation of all cation species.

Technical overview

High-energy characterization methods such as XAS and high energy resolution fluorescence detected (HERFD) XAS are commonly used for determining the concentration of cation species in 3d transition metal spinels. However, these techniques fall short of providing the complete information on the site occupation and the oxidation state of the cations. The two regions in an XAS spectrum that are generally used for this purpose are the near edge region (XANES) and the extended region (EXAFS). The XANES region of a K-edge XAS spectra consists of two peaks: the main K-edge peak (seen as sharp rise in the absorption spectra) due to $1s \rightarrow 4p$ transitions, which is dependent on the oxidation state of the central absorbing atom, and the pre-edge peak, which is due to the $1s \rightarrow 3d$ transitions and contains electronic and structural details.[37,38] The $1s \rightarrow 3d$ transitions in a centrosymmetric

coordination geometry (for example, octahedral geometry) are dipole forbidden, so if the absorbing atom is centrosymmetric then the pre-edge peak intensity is low. In the case of a non-centrosymmetric coordination geometry, *i.e.*, tetrahedral geometry, the 3d orbitals can mix with the 4p orbitals, leading to an increase in the pre-edge peak intensity. Consequently, in spinels the pre-edge peak intensity reflects the coordination geometry of the central absorbing cation[37,38] and can be used for the determination of the coordination environment surrounding the absorbing atom. The EXAFS region contains the short-range structural details around the central absorbing atom. Background-subtracted and Fourier-transformed XAS spectra in the extended region can be fitted using the EXAFS equation[39] to extract the interatomic distances and the coordination numbers for the neighbouring atoms. In addition to XAS, another high-energy method for structural study of spinels is HERFD-XAS,[40–42] a technique in which the emitted X-rays are detected over a narrow-energy bandwidth. For analysis of HERFD-XAS spectra, the emission spectra of reference standards are collected and linearly combined to fit the $K\beta_{1,3}$ emission peak of the samples to determine the ratio of the constituent species of cations. The ratio of constituent species is proportional to their contribution to the HERFD-XAS spectra, therefore, the HERFD-XAS spectra can be deconvoluted into the absorption spectra of constituent species based on the oxidation state or the spin-state.[43–46] For example, Co K-edge absorption spectra can be deconvoluted into individual Co^{2+} and Co^{3+} absorption spectra, which can then be Fourier-transformed and fitted individually to determine the short-range structure around Co^{2+} and Co^{3+}.

While these XAS and HERFD-XAS methods can provide good quantitative and qualitative details on the materials, the aforementioned techniques are inadequate for determining the site occupation of each species of cations in the case of impure spinels for the following reasons:

• The main K-edge peak is dependent only on the oxidation state of the central absorbing atom and is insensitive to the geometry of the ligands.

• Due to core-hole lifetime broadening of the 1s electron holes, the pre-edge peak is not well resolved, which limits quantitative analysis of the pre-edge to determine the concentration of cationic species in the spinel.[47]

• The pre-edge in the HERFD spectra may not be reliable if the interactions between the core-hole and the photoexcited electrons are stronger than the respective core-hole lifetime broadening. For instance, the 1s → 3d transitions in 3d transition metals may show strong interactions between the 1s and 2p orbitals in the final state.[48,49]

• The core-hole lifetime broadening due to the interaction from the photoexcited electrons (such as those in the 1s and 2p orbitals) can be avoided by first collecting the full RIXS (resonant X-ray inelastic scattering) plane in which the intensity of emitted X-rays is measured as a function of both the incident and emitted X-ray energies,[48] and then taking a line plot (by varying the incident energy at a fixed emission energy) to get the HERFD scan. However, collecting the RIXS plane requires significant time which limits its use for collecting data for a large number of samples.

• When the samples are contaminated by an impure phase, the analysis[27] of the extended region of the XAS spectra by fitting the Fourier-transformed *R*-space plots cannot be reliably used to determine the concentration of all cations species at O_h and T_d sites in spinel structures due to certain limitations and assumptions associated with the EXAFS analysis: (1) since EXAFS provides only an average site occupation, it cannot be used to differentiate between the mixed valence state of an element. (2) For ternary spinels with cation-types of similar atomic numbers as in the case of cobalt manganese oxide (the Co and Mn atoms have atomic numbers $Z = 27$ and $Z = 25$ respectively), the scattering amplitude from neighbouring Co and Mn atoms are similar, and hence EXAFS analysis cannot differentiate between Co–Co and Co–Mn scattering paths between any two given sites. In conclusion, both XAS and HERFD-XAS are inadequate and thus an alternate characterization technique is required to determine the site occupation of cations in impure spinels.

In contrast to X-ray absorption techniques, XES is a powerful but under-utilized method to determine site occupation as well as other crystal geometry and electronic features. The work on XES in the past has been limited because of the difficulty in obtaining high resolution spectra.[50] However, the development of 2nd and 3rd generation synchrotron sources with high incident flux has improved the collection of spectra, leading to higher signal to noise ratios.[44,50] XES can provide information on the cation species without the limitations of XAS because of its sensitivity to spin, oxidation states, and ligand geometry. In XES, a core hole is generated using X-rays, and the emitted fluorescence (a result of filling the core-hole) is measured. When the core-hole is filled with an electron from the 3p orbital (3p → 1s transitions), Kβ fluorescence is emitted. If the resultant hole in the 3p orbital is opposite spin with respect to the partially filled 3d orbital in 3d transition metals, the 3p–3d orbital coupling gives rise to the $K\beta_{1,3}$ peak, whereas interaction of same spin 3p hole with the partially filled 3d orbital gives rise to an additional less intense Kβ′ peak. Since the number of valence electrons are dependent on the oxidation state, interaction of the 3p hole with the valence electrons (or 3d electrons in case of transition metal oxides) makes the $K\beta_{1,3}$ spectra sensitive to the oxidation states, and the 3p–3d orbital coupling leads to spin-state sensitivity.[40,51] Furthermore, the $K\beta_{1,3}$ peak has been experimentally and theoretically shown to have sensitivity to the ligand geometry.[40,44] Different crystal field splitting energies in T_d and O_h coordination between the metal and the surrounding oxygen ligand leads to the sensitivity of the Kβ spectra to ligand geometry. Moreover, if the objective is to determine the relative concentration of cation species XES has many other advantages over XAS. Some of the advantages for XES include: (1) sample preparation for XAS includes dilution with boron nitride, whereas for XES, the pristine sample can be used for the experiment. Besides this, multiple other complications are involved in the sample preparation for XAS, such as non-uniformity, edge jump, self absorption effects, *etc.*;[39] (2) unlike XAS, XES does not require a high tunability of the incident X-rays energy and hence is not limited by the resolution of the

 This journal is © the Owner Societies 2018

monochromator; (3) XES analysis is straightforward as it involves a linear combination fitting of the $K\beta_{1,3}$ spectra, whereas for XAS, EXAFS fitting requires detailed understanding of the crystal structure of the samples; and (4) data processing and fitting of EXAFS spectra is time consuming since it requires the selection of the right set of paths for the central absorbing atoms, multiple assumptions to correlate the parameters of multiple scattering paths, determination of amplitude reduction factors for the standards, *etc.* In contrast, quantitative information can be extracted from the XES spectra by a simple linear combination fits of the standards.

Method

Diphenyl ether ($\geq$99%), dicobalt octacarbonyl (moistened with hexane (1–10%), $\geq$90% (Co)), dimanganese decacarbonyl (98%), and oleic acid ($\geq$99%) were purchased from Sigma-Aldrich. Hexane ($\geq$98.5%) and acetone ($\geq$99.5%) were purchased from EMD Millipore Corp. The precursors $Co_2(CO)_8$ and $Mn_2(CO)_{10}$ were first purified *via* sublimation at 35 °C and 65 °C, respectively, using a cold finger setup to remove any impurities which remain undissolved in diphenyl ether (DPE) during synthesis. The purified precursors were then stored under inert conditions until further use. The Co–Mn metal NPs were synthesized using a modified hot injection method.[9] A mixture of 0.1 g of oleic acid and 5.6 ml of DPE was heated under a nitrogen environment to 250 °C. The purified precursors with different molar ratios were dissolved in 3.7 ml of DPE at 60 °C, and then injected into the mixture of oleic acid and DPE at 250 °C, and allowed to react for 30 min for the nucleation and growth of the metal NPs. The reaction was then quenched in a water bath, and the products were precipitated by centrifugation in acetone anti-solvent medium. The particles were washed again in hexane and acetone solvent mixture, and the obtained precipitates were dissolved in hexane solution until further characterization. The Co/Mn ratio was determined using inductively coupled plasma mass spectroscopy (ICP-MS) on the metal NPs. For formation of oxides, the metal NPs were first dried under atmospheric conditions to remove the hexane solvent, and were then heated in air at 200 °C for 90 min.

Transmission electron microscopy (TEM) images were recorded on an FEI Tecnai T12 TEM operating at 120 kV. Synchrotron X-ray diffraction (SXRD) data was obtained at the A1 station at Cornell High Energy Synchrotron Source (CHESS). The collected diffraction patterns were integrated to obtain the intensity *vs.* 2θ, the peaks for which were aligned using a cerium standard.

XAS measurements were conducted at the bending magnet-based 20BM beamline of the Advanced Photon Source (APS) at Argonne National Laboratory. The APS is a third generation 7.0 GeV synchrotron light source providing a constant 102 mA of current (24 singlets) operating in top-up mode. The 20BM beamline of the APS uses a Si(111) double crystal monochromator for tuning the incident energy and a Rh-coated mirror for higher order harmonic rejection, and provides a flux of $\sim 10^{11}$ photons per second @ 10 keV.[52] All samples, including standards of MnO, Mn_2O_3, Mn_3O_4, CoO, Co_3O_4 $MnCo_2O_4$, and $CoMn_2O_4$, were prepared by applying a very thin layer of the powders on Kapton tape and then stacking several layers of tape to give a total absorption ($\mu(E)t$) of $\sim$1–2 absorption lengths. XAS at the manganese and cobalt K-edges, at *ca.* 6538 eV and 7709 eV respectively, were measured in transmission geometry at 45° to the X-ray beam using ion chambers upstream (I_0) and downstream (I_T) of the sample. A manganese (cobalt) reference foil was also measured simultaneously for energy calibration downstream of the sample between I_T and a reference ion chamber (I_{ref}) placed downstream of the foil. For Mn (Co) a 70/30 (30/70) sccm mixture of He/N_2 gasses was used to fill the I_0 ion chamber and 100% N_2 gas was used to fill I_T and I_{ref} ion chambers. The monochromator was tuned to full intensity *ca.* 300 eV above the absorption edge (Mn or Co) and then detuned 10% (15%) from the maximum for Mn (Co). The harmonic rejection mirror was set at an angle of 6 mrad giving a high energy cut-off of $\sim$11.2 keV. The energy steps for Mn and Co XAS scans were set to 5 eV in the pre-edge region ($E_0 - 150$ eV to $E_0 - 30$ eV), 0.3 eV in the XANES region ($E_0 - 20$ eV to $E_0 + 30$ eV), and 0.05 $Å^{-1}$ in the EXAFS region ($E_0 + 30$ eV to $E_0 + 973$ eV). For all samples and standards multiple scans (up to 10) of $\sim$14 min each were carried out at fixed sample position, which were later averaged for the analysis.

All XANES and EXAFS analysis were carried out using the IFEFFIT package.[53] The raw data was processed using ATHENA software.[53] The initial processing included deglitching of data, aligning of references, merging of scans and edge energy determination. Background subtraction was done using AUTOBK algorithm[53] following which the spectra were Fourier transformed to *R*-space and plotted as k^3-weighted spectra to obtain uniform intensity modulations, typically used for low scattering atoms.[39] Fitting for EXAFS was carried out in ARTEMIS software.[53] Theoretical crystal structures were generated using ATOMS, the parameters of which were varied to fit the experimental spectra, as a result extracting the variables of different scattering paths such as the mean square disorder, radial distance and the coordination numbers. The error values for coordination numbers and other EXAFS parameters can arise from the quality of the collected data (signal to noise ratio), data reduction, as well as the theoretical model used for the fitting. However, for comparison purposes, only the error based on the non-linear least-squared minimization to fit the *R*-space plots is used.

Co and Mn Kβ emission data were obtained at CHESS at the C1 station. The energy of the incident X-ray beam was set to 8 keV and 7 keV for Co and Mn samples, respectively, and was tuned by means of a Si(220) double-crystal monochromator. The emitted Kβ radiation was focused using five spherically bent analyser crystals aligned in Rowland geometry[54] and detected using a Pilatus 100 K area detector. Space between the spherical analysers, detector, and sample was filled with He gas to minimize attenuation of the fluorescent radiation.[55] The XES spectra were collected between 7620 eV to 7665 eV with a step size of 0.42 eV for Co samples, and 6478 eV to 6495 eV with a step size of 0.71 eV for Mn samples. For all

samples and standards multiple scans (up to 3) of ~15 min each were carried out at fixed sample position, which were then merged together to obtain the final spectra for the sample. The error values for the concentration of cation species are determined based on the least-square minimization to fit the Kβ emission data.

Results and discussion

To test the efficacy of XES and XAS in determining atomic site occupation we chose ternary spinel oxide nanoparticles (NPs). Due to the presence of additional cation species in the system, ternary spinels oxides are more complex than binary oxides (like Fe_3O_4). Thus, using ternary spinels provides a platform to highlight the differences between the two techniques in determining cation site occupation. For comparison between XAS and XES, we chose the $Co_xMn_{3-x}O_4$ spinel because each of the end members (Co_3O_4 and Mn_3O_4) are considered insulating but the mixed phases are considered semiconductors with conductivity more than an order of magnitude greater than the end members,[16,18] making this compound an interesting system to study. Our group recently found that anomalously high supercapacitor behaviour can occur when the Mn and Co content is equal, but reasons for this spike in electrochemical performance are unknown.[9] One of the historical difficulties in this system and many metal oxides is that the site occupation, and consequently the properties, are exceedingly processing-dependent for bulk materials.[16–18,56,57] As an added complication, synthesis of ternary spinels, like $Co_xMn_{3-x}O_4$, can result in monoxide impurity phases, including rock-salt CoO phase for the $Co_xMn_{3-x}O_4$ system.

To make the samples, metal Co–Mn NPs were synthesized using a modified hot injection method.[56] The metal precursors $Co_2(CO)_8$ and $Mn_2(CO)_{10}$ were first distilled to remove any impurities (see Methods for details). To obtain different stoichiometries of Co–Mn NPs, precursors with different molar ratios were dissolved in diphenyl ether (DPE) at 60 °C, and injected into a mixture of oleic acid and DPE in an inert N_2 atmosphere at 250 °C. The metal NPs are oxidized in air at 200 °C for 90 minutes to form spinel oxides, which contains an impurity phase of CoO (see Methods). To understand the effects of oxidation times we also studied an oxidation series, characterizing samples starting from zero to four hours of oxidation time. The metal NPs and oxidized NPs were characterized using transmission electron microscopy (TEM), electron diffraction (ED), and synchrotron X-ray diffraction (SXRD) to determine the size, morphology and phase. The size for the metal NPs (see Fig. S1, ESI†) before oxidation are 4.25 ± 0.55 nm, 3.75 ± 0.41 nm, 4.75 ± 0.56 nm, and 4.84 ± 0.69 nm, which after oxidation correspond to 'x' = 1.00, 1.13, 1.20, and 1.31, respectively, in the formula $Co_xMn_{3-x}O_4{\cdot}(CoO)_y$. Due to the presence of an impure CoO phase, the stoichiometry of the oxidized NPs is expressed as $Co_xMn_{3-x}O_4{\cdot}(CoO)_y$, where $Co_xMn_{3-x}O_4$ represents the pure spinel phase, and the value of 'x' is determined from XES analysis, to be discussed later.

TEM of the oxidized NPs indicate distinct spinel phases and the presence of the CoO impurity phase, as confirmed through diffraction analysis using two different representative systems of the Co : Mn molar ratios of 0.44 : 1 and 1.17 : 1. Since the exact amount of CoO phase in these two systems is not determined using XES, the stoichiometry for these two representative systems are reported based on ICP-MS values. TEM images of the oxidized NPs with Co : Mn molar ratio of 0.44 : 1 shows solid spherical particles of size 5.40 ± 1.11 nm (Fig. 1a) contaminated with clusters of larger-sized core–shell type particles (Fig. 1b). For confirmation on the phase of these large core–shell type particles, ED patterns were collected for the core–shell cluster shown in Fig. 1(b). The integrated pattern from the ED (Fig. 1c) shows that the peaks for $2\theta \sim 36^\circ$, ~43° and ~61° match well with the CoO reference standard, with the peak shoulders at $2\theta \sim 30^\circ$ and ~58° suggesting a minor contribution from the spinel phase. To understand the evolution of spinel and CoO phases as a function of oxidation time, SXRD was carried out on NPs with Co : Mn molar ratio of 1.17 : 1 oxidized at 200 °C for 0, 60, 90, and 240 minutes (Fig. 1d). A peak shoulder for the 0 min, 60 min, and 90 min samples at ~33° matches the $CoMn_2O_4$ reference peak. If there weren't any CoO impurities, these NPs with Co : Mn molar ratio of 1.17 : 1 (as determined from ICP-MS) correspond to x = 1.62. However, due to the presence of the CoO phase, for shorter oxidation times, the actual Co stoichiometry 'x' in spinel $Co_xMn_{3-x}O_4$ is smaller than the value of x = 1.62, therefore, the peak at ~33° is a closer match to the $CoMn_2O_4$ reference standard. With further oxidation, the CoO impurity oxidizes to the spinel phase, increasing the Co content in the spinel phase. This results in the peak shoulder at ~33° disappearing for the 240 min sample as the stoichiometry is now closer to the Co_2MnO_4 reference standard. The highest intensity peak at $2\theta \sim 36^\circ$ for all samples coincides with both the CoO peak and the spinel reference standards peak, so it cannot be used accurately to determine the phase of the NPs. The peak at ~43° for the unoxidized 0 min sample matches with the CoO phase, indicating a partial oxidation of the NPs upon exposure to atmospheric conditions. This peak of the unoxidized sample at ~43° reduces in intensity as the oxidation time increases, whereas, the peak at ~44° corresponding to Co_2MnO_4 spinel standard increases in intensity relative to the peak at ~43°, indicating a decrease in CoO content and an increase in spinel content with increasing oxidation time. The peak at ~61° for samples oxidized up to 90 min is present slightly shifted to lower angles as compared to the reference CoO standard peak at ~62°, however, it could correspond to either of the spinel or CoO phase. This peak at ~62° disappears for the 240 min sample, indicating presence of only the spinel phase or complete oxidation. The increase in spinel phase due to increasing oxidation time is further confirmed by the increasing peak intensity at ~64° and the new peak at ~58° for the 240 min sample, which both match the spinel phase. As we determine later using XES and EXAFS analysis, depending on the stoichiometry, up to 50% of the Co atoms are present as the CoO phase.

 This journal is © the Owner Societies 2018

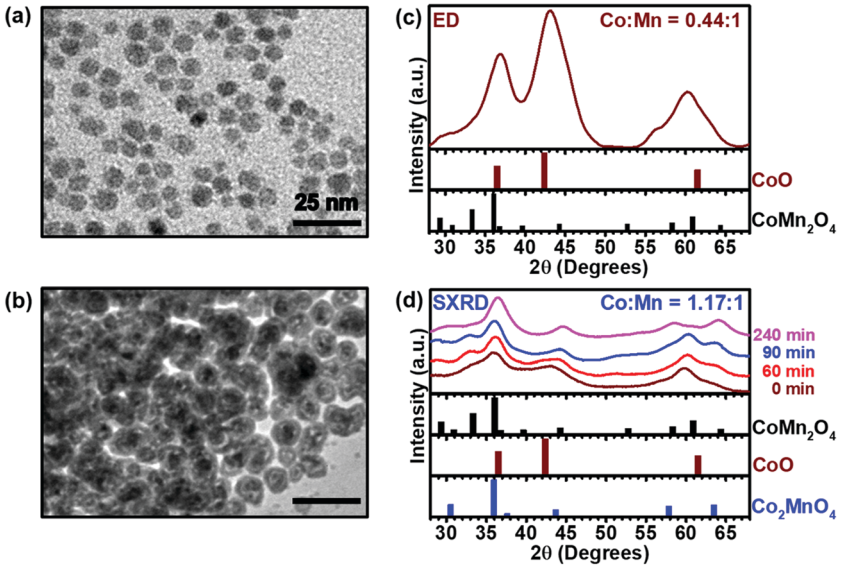

Fig. 1 Phase determination of $Co_xMn_{3-x}O_4{\cdot}(CoO)_y$ NPs after oxidation for 90 min. (a) TEM image of oxidized spherical NPs for the Co : Mn molar ratio of 0.44 : 1. (b) TEM image of a second type of core–shell NPs present in the same sample shown in (a). (c) Integrated selected area electron diffraction (ED) pattern for image shown in (b). (d) Time series synchrotron X-ray diffraction (SXRD) patterns for the Co : Mn molar ratio of 1.17 : 1 NPs oxidized in air at 200 °C. SXRD pattern along with reference standards confirm the presence of CoO phase with contribution from spinel as well. The bar patterns in (c) and (d) show the reference XRD patterns for CoO (JCPDS: 00-48-1719), $CoMn_2O_4$ (JCPDS: 01-077-0471), and Co_2MnO_4 (JCPDS: 01-084-0482). Note: 2θ scale for integrated ED is shifted to match Cu K_α.

The short-range order of the samples is probed through XAS at the Co and Mn K-edges. The normalized absorption spectra for the Co and Mn K-edges (Fig. 2a and b) show similar features in both the near-edge and the extended region, indicating that the cations exhibit similar coordination and structural environments as the Co : Mn cation ratio changes in the samples. Background removal was carried out from the absorption coefficient spectra and the obtained spectra were then Fourier-transformed and plotted as k^3-weighted R-space plots (Fig. 2c and d), plotted with open circles. For the Co K-edge R-space plots, the 1st peak at 2.0 Å and the 2nd peak at 3.15 Å correspond to the nearest neighbour oxygen atom and the nearest neighbour cation direct scattering pathway, with respect to the central Co absorbing atom. In the range of 2.50 Å to 3.75 Å, the x = 1.13 sample has multiple peaks as compared to the other stoichiometries which have only a single peak, suggesting a different coordination environment for Co in the x = 1.13 sample, possibly due to varying levels of CoO impurity between x = 1.13 and other stoichiometries. For other Co stoichiometries ($x \neq 1.13$), the 2nd peak position and FWHM remains unchanged with a minor variation in the peak intensity, indicating a similar coordination environment for Co cations. For the Mn K-edge R-space plots (Fig. 2d, plotted with open circles), the peak positions at 2.0 Å, 3.25 Å, and 3.85 Å remain unchanged for all stoichiometries besides a small variation in peak intensities, indicating that Mn is present in spinel phase. The minor variation in peak intensity is due to different relative concentrations of Mn present at O_h and T_d sites in the spinel structure.

To determine the structural parameters and the percentage site occupation of cations present at O_h and T_d sites of the spinel, and the amount of CoO present, the R-space plots are fitted to extract the variables of different scattering paths such as the radial distances and the coordination numbers. For the Co K-edge, because TEM images show both a spinel phase and a CoO phase, three different sets of scattering pathways are used for the central Co cation in the fits: (1) Co in the CoO phase, (2) Co at spinel T_d sites, and (3) Co at spinel O_h sites. Simultaneous fitting of the EXAFS spectra is conducted using these three sets of scattering paths (Fig. 2c, fit shown as solid lines). For fitting of the Mn K-edge R-space spectra, two sets of scattering pathways are used: (1) Mn at spinel O_h sites, and (2) Mn at spinel T_d sites. Simultaneous fitting of Mn EXAFS spectra is carried out using these 2 sets of scattering paths, with the fits shown as solid lines in Fig. 2(d). It is important to note that since Co and Mn have similar atomic numbers (z = 27 and z = 25, respectively), the scattering amplitude from neighbouring Co and Mn cations is assumed to be similar, and hence the Co–Co and Co–Mn scattering pathway are treated as identical.

The percentage site occupation is determined from the fitting of the EXAFS data, as reported previously.[29] Briefly, for a given stoichiometry, the experimental coordination numbers for Mn_{O_h} and Mn_{T_d} paths are nN^{Theory}_{Mn,O_h} and $(1-n)N^{Theory}_{Mn,T_d}$, where N^{Theory}_{Mn,O_h} and N^{Theory}_{Mn,T_d} are the theoretical coordination numbers for the different Mn_{O_h} and Mn_{T_d} paths, respectively, and the value of 'n' is determined from fitting the Mn K-edge EXAFS data. Therefore, the fraction of Mn cations present at spinel O_h and T_d sites equals n and $(1-n)$, respectively (Fig. 2f). Similarly, the experimental coordination numbers for Co_{CoO}, Co_{O_h}, and Co_{T_d} paths are $pN^{Theory}_{Co,CoO}$, qN^{Theory}_{Co,O_h}, and rN^{Theory}_{Co,T_d},

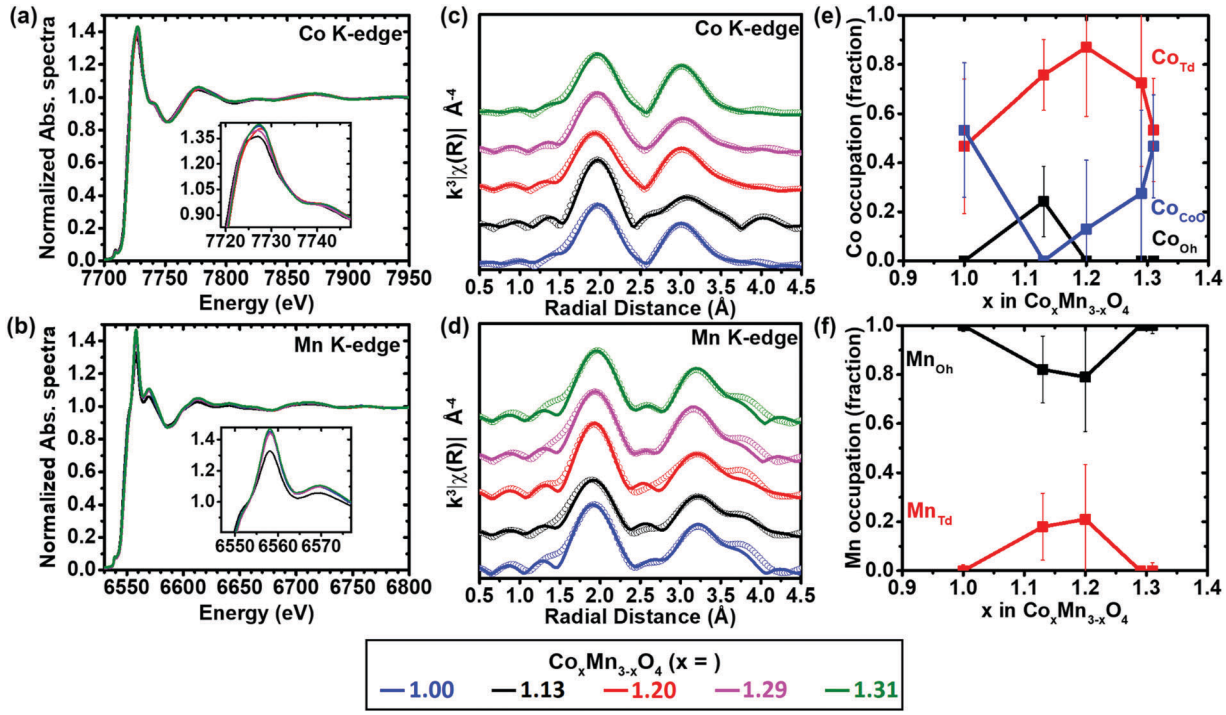

Fig. 2 (a) Co K-edge and (b) Mn K-edge XAS spectra for different stoichiometries of $Co_xMn_{3-x}O_4$ NPs contaminated with CoO impurity. (c) Co K-edge and (d) Mn K-edge Fourier transformed k^3-weighted EXAFS R-space plots (dotted lines) for different stoichiometries of $Co_xMn_{3-x}O_4$. Peaks correspond to scattering from neighbouring atoms. Fitting of R-space plots (solid lines) was carried out to determine the site occupation of (e) Co atoms present as CoO phase (O_h sites) and spinel phase (O_h and T_d sites); and (f) Mn atoms present as pure spinel phase (O_h and T_d sites).

respectively, where $N^{\text{Theory}}_{\text{Co,CoO}}$, $N^{\text{Theory}}_{\text{Co,O}_h}$ and $N^{\text{Theory}}_{\text{Co,T}_d}$ are the theoretical coordination numbers for the different Co_{CoO}, Co_{O_h} and Co_{T_d} paths, respectively, and $p + q + r = 1$, where p, q, and r are extracted from the fitting of Co K-edge EXAFS data. Similarly, the fraction of Co cations present as CoO and spinel Co_{O_h} and Co_{T_d} sites equals p, q, and r, respectively (Fig. 2e).

From the pathway analysis, the stoichiometry $x = 1.13$ has Co cations present at only spinel O_h and T_d sites and has no CoO impurity. For the $x \neq 1.13$ stoichiometries, all Co atoms octahedrally bonded to oxygen atoms are present as the CoO phase rather than at spinel O_h sites (Fig. 2e, black and blue points). Surprisingly, depending on the stoichiometry, up to ~50% of the Co atoms can exist in the impure CoO phase. In the spinel structure, the Co atoms exhibit a preference for the T_d over O_h sites as all stoichiometries besides $x = 1.13$ have no Co atoms present at O_h sites. As the Co content increases, the Co atoms move between spinel T_d sites and the CoO phase, with $x = 1.13$ having no impurity of CoO, and $x = 1.20$ having the maximum fraction of Co atoms present at spinel T_d sites. Overall, the spinel O_h sites are unoccupied by Co atoms except for the $x = 1.13$ sample. At the other extreme, the Mn cations are mostly present at O_h sites, with a maximum of 21% of Mn atoms present at spinel T_d for $x = 1.20$ (Fig. 2f). For the $x \geq 1.29$ samples, all the Mn atoms are present only at spinel O_h sites. Due to the difficulties and assumptions associated with the EXAFS fittings, as discussed earlier, the error for experimental coordination numbers (shown as vertical bars in Fig. 2e and f) has an average of 16% and a maximum of as high as 34%. In summary, analysis of the extracted site occupation data shows that the Co atoms prefer to sit at spinel T_d sites, and the Mn atoms prefer to sit at spinel O_h sites; the incomplete occupation of Co and Mn at their preferred sites (T_d and O_h, respectively) indicates a mixed site occupancy.

Although EXAFS characterization is a powerful tool that is used to resolve the local atomic arrangements and structure, XAS analysis is not sufficient to determine the ratio of metal cations present as 2+ and 3+ oxidation states at O_h sites of the spinel. Therefore, we conduct a cation site-selective study of the $Co_xMn_{3-x}O_4$ system by taking advantage of the spin, oxidation state and ligand sensitive $K\beta_{1,3}$ spectra obtained using XES. Previous studies[43–46] have shown that the XES spectra of a sample is a linear combination of the $K\beta_{1,3}$ spectra of its constituent cation species. Since the spot size of the incident beam used for the excitation of the core-electron is on the order of a millimetre, multiple independent core-hole generation events occur simultaneously, therefore, the collected XES spectra is a combination of the XES spectra of each independent core-hole filling event. Since a given cation species has a fixed XES spectra, the collected XES spectra can be defined as a weighted linear combination of all the constituent species in the system. The bulk reference standards (shown in Table 1), which have similar oxidation state and coordination environment as that of the various cation species present in the $Co_xMn_{3-x}O_4$ NPs, are linearly combined to determine the concentration of each cation species present in the system. As an example, the normalized Co-$K\beta_{1,3}$ spectra for $Co_{1.13}Mn_{1.87}O_4$

 This journal is © the Owner Societies 2018

Table 1 Bulk reference standards having similar oxidation state and coordination environment as that of various cation species present in the $Co_xMn_{3-x}O_4$ NPs

Geometry	Cation species	Reference standard
Tetrahedral	Co^{2+}	$CoCr_2O_4$
	Mn^{2+}	$MnAl_2O_4$
Octahedral	Co^{2+}	CoO
	Co^{3+}	$ZnCo_2O_4$
	Mn^{2+}	MnO
	Mn^{3+}	$ZnMn_2O_4$

NPs are fitted with Co-K$\beta_{1,3}$ bulk reference standards spectra, shown as dotted lines in Fig. 3(a). It is, however, important to note that the linear combination depends on the availability of the right set of standards, *i.e.*, cations with the same oxidation state, ligand geometry, and spin-state as that of the cation species present in the sample. The normalized ratio of intensities for the standards is proportional to the relative concentration of the three species of Co cations present in the NPs (Co^{2+} cations tetrahedrally bonded to oxygen atoms, and Co^{2+} and Co^{3+} cations octahedrally bonded to oxygen atoms). CoO present as impurities in the NPs consists of Co^{2+} octahedrally bonded to oxygen atoms. Since the Co atoms in CoO have a similar coordination environment and ligand geometry as Co^{2+} present at O_h sites of the spinel ($Co_{O_h}^{2+}$), the contribution from the bulk CoO standard is mathematically deconvoluted to determine the concentration of Co_{CoO}^{2+} and $Co_{O_h}^{2+}$ cation species, and thus the value of 'x' in $Co_xMn_{3-x}O_4$ for each sample, discussed in detail in the ESI.† The Mn-K$\beta_{1,3}$ spectra for bulk reference standards are linearly combined to fit the Mn-K$\beta_{1,3}$ spectra for $Co_{1.13}Mn_{1.87}O_4$ NPs, shown as a dotted line in Fig. 3(b). Initial fitting of the Mn-K$\beta_{1,3}$ spectra for all samples included an additional fourth reference standard MnO_2, *i.e.*, Mn^{4+} octahedrally bonded to oxygen atoms, however, its contribution is negligible[9] and shows higher error when included in the fitting, so it is excluded from the fits (see Fig. S3, ESI†). The results from both Co and Mn edges fittings are plotted in Fig. 3(c and d), in terms of the concentration of all species of cations. The concentration of $Co_{O_h}^{2+}$ remains relatively constant, however, analytical deconvolution (see ESI†) shows that for x = 1.13, all $Co_{O_h}^{2+}$ are present at only the spinel O_h sites, whereas for other stoichiometries ($x \neq 1.13$) all $Co_{O_h}^{2+}$ are present as just the CoO phase. For $x \geq 1.13$, the relative concentration of $Co_{O_h}^{3+}$ (and $Mn_{O_h}^{3+}$) increases with a concomitant decrease in $Co_{T_d}^{2+}$ (and $Mn_{T_d}^{2+}$), implying that as the Co content increases in the NPs the Co and Mn cations move from spinel T_d to spinel O_h sites with an increase in the oxidation state. Mn edge analysis shows that $Mn_{O_h}^{3+}$ is the dominant species, however, both 2+ and 3+ oxidation state Mn cations are present at spinel O_h sites, unlike the Co cations, which has only 3+ cations at spinel O_h sites. For the higher stoichiometries ($x \geq 1.29$), all Mn atoms are present at O_h sites with 3+ oxidation state due to preferential site occupation of all the Co cations at T_d sites. The error in the relative concentrations of different cation species as determined from least square fitting is in the range of 0 to 12%, with the average error being 3.5%, significantly lower than the average error of 16% in EXAFS analysis.

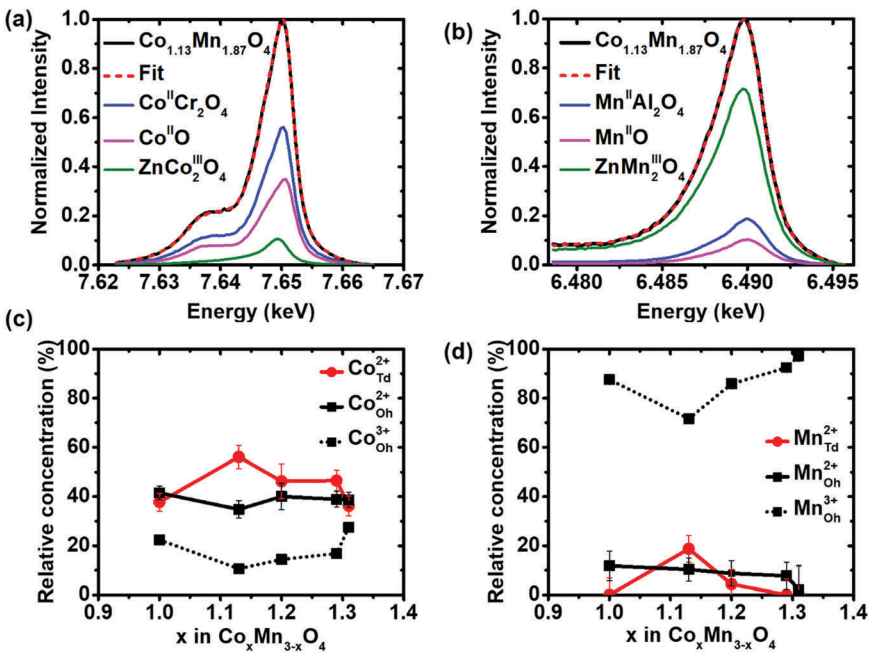

Fig. 3 Spin, oxidation state and ligand sensitive K$\beta_{1,3}$ (3p → 1s) spectra are obtained using XES for different stoichiometries of $Co_xMn_{3-x}O_4$ NPs contaminated with CoO impurities. XES spectra of the sample are fitted using linear combination of K$\beta_{1,3}$ spectra of bulk reference standards to determine the relative concentration of each constituent cationic species. Figure shows the XES spectra and the fitting of $Co_{1.13}Mn_{1.87}O_4$ NPs for (a) Co-K$\beta_{1,3}$ edge and (b) Mn-K$\beta_{1,3}$ edge. Superscripts represent the oxidation state of cations in the standards. Relative concentration of different cation species for (c) Co cations and (d) Mn cations. Note: Co_{Oh}^{2+} cations are present in both CoO and spinel phase.

Direct extraction of site occupation of cations from analysis of XES spectra has not been reported before, therefore, to validate the accuracy of XES, we compare the results obtained from XES with those from EXAFS (summarized in Fig. 4a). As shown in the diagram, EXAFS analysis provides only the percentage of site occupation for Co and Mn cations at O_h and T_d sites, whereas XES analysis provides the additional information on the oxidation state of cations as demonstrated in Fig. 3. For example, for Co, EXAFS gives the percentage of Co atoms sitting at O_h and T_d sites (*i.e.*, Co_{T_d} and Co_{O_h}), whereas using XES it is possible to determine the percentage site occupation for each Co species, *i.e.*, $Co_{T_d}^{2+}$, $Co_{O_h}^{2+}$, and $Co_{O_h}^{3+}$. Fig. 4(b–d) show the comparison between the site occupation data obtained using XES (purple points) and EXAFS (blue points) for the samples for Mn_{O_h}, Co_{O_h}, and Co as CoO (Fig. 4b, c and, d, respectively). The insets in Fig. 4(b–d) are the percentage error for XES and EXAFS for each sample. The source of errors includes the uncertainties associated with the data acquisition and the data reduction. However, for quantification and comparison between the two the analysis techniques, the error values presented here for both EXAFS and XES analysis are limited to the least-square minimization to fit the *R*-space and the K-β spectra, respectively. To more directly compare the values obtained using EXAFS and those from XES, the XES data is depicted as the sum of the concentration of the two species of Mn cations present at O_h sites-$Mn_{O_h}^{2+}$ and $Mn_{O_h}^{3+}$. For Mn site occupation at O_h sites both EXAFS and XES show similar trends (Fig. 4b), with the majority of Mn atoms present at O_h sites for all stoichiometries. The $x = 1.20$ sample shows a larger difference between the two techniques because of the high errors associated with the EXAFS analysis. The average error for Mn site occupation at O_h sites as determined from EXAFS is ~9%, whereas for XES, the average error is ~7%. EXAFS shows errors as high as 22% for Mn site occupation, whereas for XES, the error determined is consistently smaller than 12% (Fig. 4b inset). The percentage Co atoms present at O_h sites with both XES and EXAFS shows a similar trend (Fig. 4c). However, based on EXAFS analysis, no Co atoms are present at O_h sites except for $x = 1.13$ which contains ~25%, whereas XES shows the presence of Co at O_h sites for all samples except for $x = 1.00$. This disparity could be due to the greater accuracy and smaller error in the XES analysis. The error for the percentage of Co atoms at O_h sites is ~14.4% from EXAFS and ~1.3% from XES analysis (Fig. 4c inset). The percentage of Co atoms present as CoO phase are shown in Fig. 4(d). Again, results from both methods follow similar trends over the composition range but the XES values are slightly higher for $x > 1.13$. Both XES and EXAFS show significant amounts (up to 50%) of Co atoms present as impure CoO phase. The average error from EXAFS and XES for Co present as CoO phase are ~22% and ~1%, respectively. The error observed for the Co present as CoO is as high as 34% in the case of EXAFS analysis, which makes the results obtained ambiguous for certain stoichiometries. However, error from XES analysis is consistently smaller than 2% for all stoichiometries (Fig. 4d inset). Therefore, in conclusion, both XES and

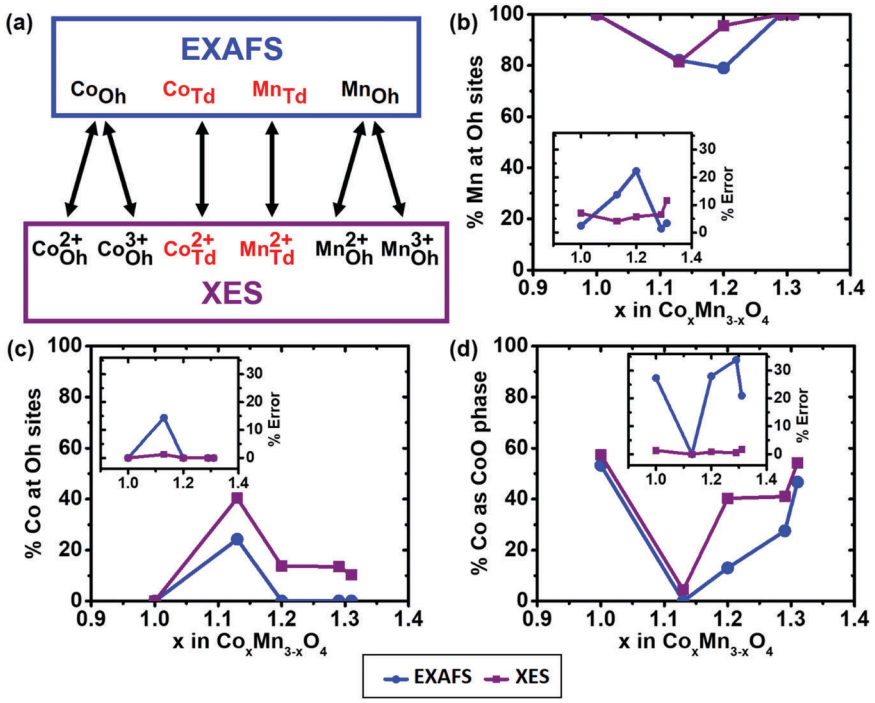

Fig. 4 Correlation between site occupation of Mn and Co cations obtained using EXAFS and XES. (a) Summarizes the information that can be extracted using the two techniques. Comparison of site occupation between EXAFS and XES for (b) % Mn atoms present at O_h sites, (c) % Co atoms present at O_h sites, and (d) % Co atoms present as CoO. The remaining Co and Mn atoms are present at T_d sites of spinel (not shown). Inset shows the % error for values obtained using EXAFS and XES.

This journal is © the Owner Societies 2018

EXAFS show similar site occupation numbers and trends, however, XES has consistently and significantly lower errors. It is readily apparent that the XES error is lower than the EXAFS error in all cases, by up to ~20%, implying that XES is more reliable and an efficient technique to determine the site occupation of cations in the NPs.

Conclusions

Elucidating the cation distribution in spinels has been a persistent problem in materials science. Under different synthetic and post-processing conditions, cation site occupation can deviate from the intrinsic preference for a completely normally or inversely distributed spinel. Such disorder in cation distribution complicates the determination and prediction of physical properties and hence, it is necessary to look for an accessible tool in which the cation distribution information, including atom types and their valence states, can be extracted accurately. In this study, we exploited the acute sensitivity of XES $K\beta_{1,3}$ emission lines to the spin, ligand geometry, and oxidation state to report the cation site occupation of spinel $Co_xMn_{3-x}O_4$ contaminated with CoO. By combining the spectra of bulk reference standards which represent different oxidation states and coordination environment, the concentrations of all existing cation species at their respective sites were determined. This determination of cation oxidation states is not achievable through the widely used method of K-edge XAS. In fact, the high errors from the many assumptions employed in XAS limit the accuracy of the extracted occupation information. To validate the ability of XES in extracting site occupation, results from XES are further compared to the EXAFS analysis of the XAS spectra. As revealed by both techniques, the occupation of Mn atoms at octahedral sites is nearly 100%, and the occupation of Co atoms shows a local maximum at $x = 1.13$ for spinel octahedral sites and a local minimum at $x = 1.13$ for CoO octahedral sites. The average uncertainty in site occupation data obtained using XES is ~3.5% whereas from EXAFS, the average uncertainty is ~16%, significantly greater than XES. The agreement of the XES data to the EXAFS analysis, as well as the unveiled oxidation states of the atoms at different sites, are all clear and solid evidence to the superiority of XES over conventional techniques such as XAS.

Conflicts of interest

There are no conflicts to declare.

Acknowledgements

This work was supported in part by the National Science Foundation (NSF) under award number DMR-1809429, DMR-1149036, and CHE-1507753. This work made use of Cornell Centre for Materials Research (CCMR) and Cornell High Energy Synchrotron Source (CHESS) facilities, and was funded in part by National Science Foundation under award number DMR-1719875 and DMR-1332208, respectively. We thank Andrew Nelson for his help with the SXRD, synthesis and sample preparation. CLS@APS facilities (Sector 20-BM) at the Advanced Photon Source (APS) are supported by the U.S. Department of Energy (DOE), NSERC Canada, the University of Washington, the Canadian Light Source (CLS), and the APS. Use of the APS is supported by the DOE under Contract No. DE-AC02-06CH11357. The CLS is financially supported by NSERC Canada, CIHR, NRC, and the University of Saskatchewan.

References

1 P. W. Menezes, A. Indra, N. R. Sahraie, A. Bergmann, P. Strasser and M. Driess, *ChemSusChem*, 2015, **8**, 164–167.
2 F. Tielens, M. Calatayud, R. Franco, J. M. Recio, J. Pérez-Ramírez and C. Minot, *J. Phys. Chem. B*, 2006, **110**, 988–995.
3 H. T. Zhang and X. H. Chen, *Nanotechnology*, 2006, **17**, 1384–1390.
4 B. Mehdaoui, R. Moubah, B. Orayech, M. Bahout, O. Peña, M. Jáuregui, D. Saurel and A. El Bouari, *J. Alloys Compd.*, 2018, **748**, 528–536.
5 C. Wei, Z. Feng, G. G. Scherer, J. Barber, Y. Shao-Horn and Z. J. Xu, *Adv. Mater.*, 2017, **29**, 1–8.
6 C. H. Kim, Y. Myung, Y. J. Cho, H. S. Kim, S.-H. Park, J. Park, J.-Y. Kim and B. Kim, *J. Phys. Chem. C*, 2009, **113**, 7085–7090.
7 H. Kawazoe and K. Ueda, *J. Am. Ceram. Soc.*, 1999, **36**, 3330–3336.
8 F. Cheng, J. Shen, B. Peng, Y. Pan, Z. Tao and J. Chen, *Nat. Chem.*, 2011, **3**, 79–84.
9 S. D. Perera, X. Ding, A. Bhargava, R. Hovden, A. Nelson, L. F. Kourkoutis and R. D. Robinson, *Chem. Mater.*, 2015, **27**, 7861–7873.
10 D. S. McClure, *J. Phys. Chem. Solids*, 1957, **3**, 311–317.
11 Z. J. Zhang, Z. L. Wang, B. C. Chakoumakos and J. S. Yin, *J. Am. Chem. Soc.*, 1998, **120**, 1800–1804.
12 J. C. Waerenborgh, M. O. Figueiredo, J. M. P. Cabral and L. C. J. Pereira, *J. Solid State Chem.*, 1994, **111**, 300–309.
13 Q. Zhao, Z. Yan, C. Chen and J. Chen, *Chem. Rev.*, 2017, **117**, 10121–10211.
14 H. S. C. O'Neill and A. Navrotsky, *Am. Mineral.*, 1983, **68**, 181–194.
15 A. Zakutayev, T. R. Paudel, P. F. Ndione, J. D. Perkins, S. Lany, A. Zunger and D. S. Ginley, *Phys. Rev. B: Condens. Matter Mater. Phys.*, 2012, **85**, 1–8.
16 A. Rousset, C. Tenailleau, P. Dufour, H. Bordeneuve, I. Pasquet, S. Guillemet-Fritsch, V. Poulain and S. Schuurman, *Int. J. Appl. Ceram. Technol.*, 2013, **10**, 175–185.
17 H. Han, J. S. Lee, J. H. Ryu, K. M. Kim, J. L. Jones, J. Lim, S. Guillemet-Fritsch, H. C. Lee and S. Mhin, *J. Phys. Chem. C*, 2016, **120**, 13667–13674.
18 T. Brylewski, W. Kucza, A. Adamczyk, A. Kruk, M. Stygar, M. Bobruk and J. Dąbrowa, *Ceram. Int.*, 2014, **40**, 13873–13882.
19 A. M. Stoneham, *IEEE Trans. Dielectr. Electr. Insul.*, 1997, **4**, 604–613.
20 I. G. Austin and N. F. Mott, *Adv. Phys.*, 2001, **50**, 757–812.

21 D. M. Smyth, *The Defect Chemistry of Metal Oxides*, Oxford University Press, New York, 2000.
22 J. F. Hochepied, P. Sainctavit and M. P. Pileni, *J. Magn. Magn. Mater.*, 2001, **231**, 315–322.
23 Z. Huang, W. Zhou, C. Ouyang, J. Wu, F. Zhang, J. Huang, Y. Gao and J. Chu, *Sci. Rep.*, 2015, **5**, 2–9.
24 F. Zhang, P. Wang, J. Koberstein, S. Khalid and S. W. Chan, *Surf. Sci.*, 2004, **563**, 74–82.
25 D. Ha, A. H. Caldwell, M. J. Ward, S. Honrao, K. Mathew, R. Hovden, M. K. A. Koker, D. A. Muller, R. G. Hennig and R. D. Robinson, *Nano Lett.*, 2014, **14**, 7090–7099.
26 L. M. Moreau, D. Ha, H. Zhang, R. Hovden, D. A. Muller and R. D. Robinson, *Chem. Mater.*, 2013, **25**, 2394–2403.
27 D. Ha, L. M. Moreau, S. Honrao, R. G. Hennig and R. D. Robinson, *J. Phys. Chem. C*, 2013, **117**, 14303–14312.
28 D.-H. Ha, L. M. Moreau, C. R. Bealing, H. Zhang, R. G. Hennig and R. D. Robinson, *J. Mater. Chem.*, 2011, **21**, 11498–11510.
29 L. M. Moreau, D. H. Ha, C. R. Bealing, H. Zhang, R. G. Hennig and R. D. Robinson, *Nano Lett.*, 2012, **12**, 4530–4539.
30 P. E. R. Blanchard, A. P. Grosvenor, R. G. Cavell and A. Mar, *J. Mater. Chem.*, 2009, **19**, 6015.
31 S. A. Pizarro, P. Glatzel, H. Visser, J. H. Robblee, G. Christou, U. Bergmann and V. K. Yachandra, *Phys. Chem. Chem. Phys.*, 2004, **6**, 4864–4870.
32 H. Visser, E. Anxolabéhère-Mallart, U. Bergmann, P. Glatzel, J. H. Robblee, S. P. Cramer, J.-J. Girerd, K. Sauer, M. P. Klein and V. K. Yachandra, *J. Am. Chem. Soc.*, 2001, **123**, 7031–7039.
33 P. Simon and Y. Gogotsi, *Nat. Mater.*, 2008, **7**, 845–854.
34 J. R. Miller and P. Simon, *Science*, 2008, **321**, 651–652.
35 J. Zhang, L. Wang, L. Xu, X. Ge, X. Zhao, M. Lai, Z. Liu and W. Chen, *Nanoscale*, 2015, **7**, 720–726.
36 Y. Liang, H. Wang, J. Zhou, Y. Li, J. Wang, T. Regier and D. Hongjie, *J. Am. Chem. Soc.*, 2012, **134**, 3517–3523.
37 F. Farges, Y. Lefrère, S. Rossano, A. Berthereau, G. Calas and G. E. Brown, *J. Non-Cryst. Solids*, 2004, **344**, 176–188.
38 M. Bauer, T. Kauf, J. Christoffers and H. Bertagnolli, *Phys. Chem. Chem. Phys.*, 2005, **7**, 2664–2670.
39 S. Calvin, *XAFS for Everyone*, CRC Press, 2013.
40 P. Glatzel, M. Sikora, G. Smolentsev and M. Fernández-García, *Catal. Today*, 2009, **145**, 294–299.
41 O. V. Safonova, M. Tromp, J. A. van Bokhoven, F. M. F. de Groot, J. Evans and P. Glatzel, *J. Phys. Chem. B*, 2006, **110**, 16162–16164.
42 P. Eisenberger, P. M. Platzman and H. Winick, *Phys. Rev. Lett.*, 1976, **36**, 623–626.
43 A. Bordage, V. Trannoy, O. Proux, H. Vitoux, R. Moulin and A. Bleuzen, *Phys. Chem. Chem. Phys.*, 2015, **17**, 17260–17265.
44 G. Peng, X. Wang, M. M. Crush, S. P. Cramer, F. M. F. DeGroot, K. Hämäläinen, J. A. Moore, J. B. Hastings, D. P. Siddons, W. H. Armstrong and O. C. Mullins, *J. Am. Chem. Soc.*, 1994, **116**, 2914–2920.
45 P. Glatzel, L. Jacquamet, Y. Bergmann, F. M. F. de Groot and S. P. Cramer, *Inorg. Chem.*, 2002, **41**, 3121.
46 N. Matoussevitch, H. Bo and P. Glatzel, *Inorg. Chem.*, 2014, **53**, 8367–8375.
47 W. M. Heijboer, P. Glatzel, K. R. Sawant, R. F. Lobo, U. Bergmann, R. A. Barrea, D. C. Koningsberger, B. M. Weckhuysen and F. M. F. De Groot, *J. Phys. Chem. B*, 2004, **108**, 10002–10011.
48 P. Glatzel, T.-C. Weng, K. Kvashnina, J. Swarbrick, M. Sikora, E. Gallo, N. Smolentsev and R. A. Mori, *J. Electron Spectrosc. Relat. Phenom.*, 2013, **188**, 17–25.
49 K. O. Kvashnina, S. M. Butorin and P. Glatzel, *J. Anal. At. Spectrom.*, 2011, **26**, 1265.
50 P. Glatzel and U. Bergmann, *Coord. Chem. Rev.*, 2005, **249**, 65–95.
51 M. Bauer, *Phys. Chem. Chem. Phys.*, 2014, **16**, 13827–13837.
52 S. M. Heald, D. L. Brewe, E. A. Stern, K. H. Kim, F. C. Brown, D. T. Jiang, E. D. Crozier and R. A. Gordon, *J. Synchrotron Radiat.*, 1999, **6**, 347–349.
53 B. Ravel and M. Newville, *J. Synchrotron Radiat.*, 2005, **12**, 537–541.
54 N. Lee, T. Petrenko, U. Bergmann, F. Neese and S. Debeer, *J. Am. Chem. Soc.*, 2010, **132**, 9715–9727.
55 K. M. Lancaster, K. D. Finkelstein and S. Debeer, *Inorg. Chem.*, 2011, **50**, 6767–6774.
56 E. Rios, J.-L. Gautier, G. Poillerat and P. Chartier, *Electrochim. Acta*, 1998, **44**, 1491–1497.
57 J. F. Marco, J. R. Gancedo, M. Gracia, J. L. Gautier, E. Ríos and F. J. Berry, *J. Solid State Chem.*, 2000, **153**, 74–81.

 This journal is © the Owner Societies 2018